Boundary Effects of Weak Nonlocality in Multilayered Dielectric Metamaterials

Giuseppe Castaldi,[1] Andrea Alù,[2,3,4] and Vincenzo Galdi[1,*]

[1]*Fields & Waves Lab, Department of Engineering, University of Sannio, 82100 Benevento, Italy*

[2]*Photonics Initiative, Advanced Science Research Center, City University of New York, New York, New York 10031, USA*

[3]*Physics Program, Graduate Center, City University of New York, New York, New York 10026, USA*

[4]*Department of Electrical Engineering, City College of New York, New York, New York 10031, USA*

Nonlocal (spatial-dispersion) effects in multilayered metamaterials composed of periodic stacks of alternating, deeply subwavelength dielectric layers are known to be negligibly weak. Counterintuitively, under certain critical conditions, *weak nonlocality* may build up *strong boundary effects* that are not captured by conventional (local) effective-medium models based on simple mixing formulas. Here we show that this phenomenon can be fruitfully studied and understood in terms of error propagation in the iterated maps of the trace and antitrace of the optical transfer matrix of the multilayer. Our approach effectively parameterizes these peculiar effects via remarkably simple and insightful closed-form expressions, which enable direct identification of the critical parameters and regimes. We also show how these boundary effects can be captured by suitable nonlocal corrections.

I. INTRODUCTION

Away from the quantum regime, the macroscopic electromagnetic response of material media is typically modeled via constitutive relationships featuring a set of intensive properties, such as dielectric permittivity, electrical conductivity, and magnetic permeability [1]. Although these quantities clearly depend on the fine (atomic and molecular) structure of the medium, they do not punctually describe the strong field fluctuations on such fine scales, but describe only some suitably averaged behavior.

Besides being a cornerstone of the electrodynamics of continuous media [1], the above-mentioned *homogenization* concept is also heavily applied to the description of "metamaterials" (i.e., composite materials made of subwavelength-sized (dielectric or metallic) inclusions in a host medium), which can be purposely designed to exhibit specific desired properties [2,3].

In their arguably simplest conceivable form, homogenized models are based on mixing formulas (e.g., Maxwell Garnett formula) that essentially depend on the inclusions' material constituents as well as their shapes, orientations, and filling fractions, but not on their specific sizes and spatial arrangement [4]. Such *effective-medium theory* (EMT) is known to work especially well for dielectric structures featuring electrically small inclusions, whereas it may become significantly inaccurate in the presence of metallic constituents and or inclusions with moderate electrical sizes. In these last cases, *nonlocal* corrections (in the form of spatial derivatives of the fields or, equivalently, wavevector dependence in the constitutive relationships) are typically needed to account for the arising spatial dispersion (see, e.g., Refs. [5–9]).

Contrary to the conventional wisdom above, Herzig Sheinfux et al. [10] recently pointed out a deceptively simple example of an *all-dielectric* multilayered metamaterial featuring *deeply subwavelength* layers that may exhibit peculiar boundary effects that are not captured by standard (local) EMT approaches. More specifically, under certain critical illumination conditions, the optical transmission (and reflection) of a finite-thickness slab of such metamaterial may differ substantially from the local EMT prediction, and may become ultrasensitive to the spatial order and/or size of the layers as well as to the addition or removal of a very thin layer (see also Ref. [11]). These counterintuitive effects, experimentally demonstrated by Zhukovsky et al. [12], have been attributed to the peculiar (interface-dominated) phase-accumulation mechanism in the structure [10], and have been shown to be potentially captured by suitable (possibly nonlocal and bianisotropic) corrections [13,14].

Besides the inherent academic interest in the homogenization aspects, the ultrasensitivity phenomenon described above may open intriguing avenues in applications such as optical sensing and switching [10,11]. Moreover, similar mechanisms have also been shown to play a key

———————
*[*]vgaldi@unisannio.it

role in establishing Anderson localization in disordered nanophotonic structures [15,16].

Against the background above, in this paper, we propose a simple and physically incisive modeling of the boundary effects that can be induced by weak nonlocality in multilayered dielectric metamaterials. Our approach, based on the trace-and-antitrace-map formalism [17], directly relates the geometrical and constitutive parameters of interest to a set of meaningful observables through simple closed-form expressions. Besides elucidating the underlying mechanisms, this directly enables the identification of critical parameters and regimes, and naturally suggests possible nonlocal corrections capable of capturing the effects.

Accordingly, the rest of the paper is structured as follows. In Sec. II, we introduce the problem geometry and background, and outline the mathematical formulation of our approach. In Sec. III, we apply the approach to the analytical modeling of the boundary effects induced by weak nonlocality, and identify two distinct mechanisms. Moreover, we illustrate some representative results, and also explore possible nonlocal corrections. Finally, in Sec. IV, we provide some concluding remarks and perspectives. Ancillary technical derivations are detailed in four appendices.

II. BACKGROUND AND MATHEMATICAL FORMULATION

A. Geometry

Referring to the schematic in Fig. 1, as in Ref. [10], we consider a multilayered metamaterial consisting of a periodic arrangement of alternating dielectric layers (of infinite extent in the x-y plane, and stacked along the z direction), with relative permittivities ε_a and ε_b and thicknesses d_a and d_b, respectively. More specifically, we consider a structure of finite thickness L made of n unit cells (bilayers) embedded in a homogeneous medium with relative permittivity ε_e, illuminated by a time-harmonic [$\exp(-i\omega t)$], transverse-electric (TE) polarized plane wave with y-directed electric field, impinging from the exterior medium at an angle θ with respect to the z axis. Accordingly, the relevant components of the impinging wavevector $\mathbf{k}_e$ can be expressed as

$$k_{ze} = k\sqrt{\varepsilon_e}\cos\theta, \quad k_x = k\sqrt{\varepsilon_e}\sin\theta, \quad (1)$$

with $k = \omega/c$ denoting the vacuum wavenumber (and c the corresponding wave speed), and k_x subject to momentum conservation [18]. In what follows, we assume there are propagating fields in the exterior medium (i.e., real-valued incidence angles θ), lossless dielectric materials (i.e., real-valued, positive $\varepsilon_a, \varepsilon_b, \varepsilon_e$), and deeply subwavelength layer thicknesses (i.e., $d_a, d_b \ll \lambda$, with $\lambda = 2\pi/k$ denoting the vacuum wavelength).
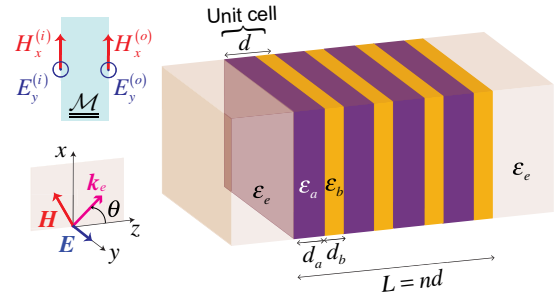

FIG. 1. Problem geometry. A multilayered metamaterial composed of alternating dielectric layers, with relative permittivities ε_a and ε_b and thicknesses d_a and d_b, respectively. The structure is assumed to be of infinite extent in the x-y plane and of finite thickness ($L = nd$) along the z direction, and is embedded in a homogeneous medium with relative permittivity ε_e. The two insets on the left illustrate the transfer-matrix formalism [top, see Eq. (4)] and the TE-polarized plane-wave illumination (bottom).

As will be clearer hereafter, our assumption of considering the same exterior medium at the two ends of the metamaterial slab, although slightly less general than that in previous studies [10,13,14], allows an effective description of the underlying physical mechanisms in terms of a minimal number of parameters. Dealing with a more general scenario featuring two different exterior media implies only formal complications, but it does not add significant physical insight into the phenomenon.

B. Local EMT formulation

Following the standard (local) EMT formulation [4], the above-mentioned multilayered metamaterial can be modeled in terms of a homogenized, uniaxially anisotropic medium. For the assumed TE polarization, the relevant (in-plane) component of the resulting relative-permittivity tensor is given by [4]

$$\bar{\varepsilon}_\parallel = f_a\varepsilon_a + f_b\varepsilon_b, \quad (2)$$

with $f_a = d_a/d$ and $f_b = d_b/d = 1 - f_a$ denoting the filling fractions of the two material constituents, and $d = d_a + d_b$ the unit-cell thickness. Here and henceforth, the overbar is used to tag EMT-based quantities. In such an effective medium, the longitudinal wavenumber is given by

$$\bar{k}_z = \sqrt{k^2\bar{\varepsilon}_\parallel - k_x^2}, \quad (3)$$

with the (conserved) transverse component k_x already defined in Eq. (1).

C. Transfer-matrix formalism

Our approach exploits as a rigorous reference solution the well-known transfer-matrix method (see Chap. 1 in Ref. [18]). As illustrated in the inset in Fig. 1, for the

assumed TE polarization, the tangential field components at two interfaces of a layer can be related via

$$\begin{bmatrix} E_y^{(i)} \\ iZ_e H_x^{(i)} \end{bmatrix} = \underline{\underline{\mathcal{M}}} \cdot \begin{bmatrix} E_y^{(o)} \\ iZ_e H_x^{(o)} \end{bmatrix}, \qquad (4)$$

where the superscripts (i) and (o) denote the input and output interfaces, respectively, $\underline{\underline{\mathcal{M}}}$ is a *unimodular*, dimensionless 2×2 transfer matrix, and

$$Z_e = \frac{\omega \mu_0}{k_{ze}} \qquad (5)$$

represents the TE wave impedance in the exterior medium, with μ_0 denoting the vacuum magnetic permeability and k_{ze} already defined in Eq. (1). When multiple layers are cascaded, by iterating the above representation, we can obtain the resulting transfer matrix via the chain product of the matrices representing the single layers (see Chap. 1 in Ref. [18]). Thus, for example, the transfer matrix pertaining to a unit cell as in Fig. 1 is given by

$$\underline{\underline{\mathcal{M}}}_{ab} = \underline{\underline{\mathcal{M}}}_a \cdot \underline{\underline{\mathcal{M}}}_b, \qquad (6)$$

with the expressions of the matrices $\underline{\underline{\mathcal{M}}}_a$ and $\underline{\underline{\mathcal{M}}}_b$ explicitly given in Appendix A. Likewise, the transfer matrix pertaining to a multilayer composed of n unit cells is straightforwardly obtained via a nth power: viz.,

$$\underline{\underline{\mathcal{M}}}_n = \underline{\underline{\mathcal{M}}}_{ab}^n. \qquad (7)$$

From the transfer matrices in Eqs. (6) and (7), the optical response of the multilayered metamaterial can be fully characterized, in terms of both a Bloch-type dispersion relationship (in the infinite periodic limit) and transmission and/or reflection (for a finite number of layers) (see Chap. 1 in Ref. [18]).

D. Trace and antitrace maps

For the study of some fundamental aspects of the optical response of a multilayered metamaterial, two suitable combinations of the transfer-matrix elements, known as "trace" and "antitrace," are sufficient [17]. For a generic 2×2 matrix

$$\underline{\underline{\mathcal{M}}} = \begin{bmatrix} \mathcal{M}_{11} & \mathcal{M}_{12} \\ \mathcal{M}_{21} & \mathcal{M}_{22} \end{bmatrix}, \qquad (8)$$

they are defined as [19]

$$\mathrm{Tr}\left(\underline{\underline{\mathcal{M}}}\right) \equiv \mathcal{M}_{11} + \mathcal{M}_{22}, \qquad (9a)$$

$$\mathrm{Atr}\left(\underline{\underline{\mathcal{M}}}\right) \equiv \mathcal{M}_{21} - \mathcal{M}_{12}, \qquad (9b)$$

respectively. For the periodic multilayer of interest here, if we let

$$\chi_n \equiv \mathrm{Tr}\left(\underline{\underline{\mathcal{M}}}_{ab}^n\right), \quad \upsilon_n \equiv \mathrm{Atr}\left(\underline{\underline{\mathcal{M}}}_{ab}^n\right), \qquad (10)$$

it can be shown [17] that the Bloch-type dispersion relationship (infinite number of layers) is given by

$$\cos\left(k_z d\right) = \frac{\chi_1}{2}. \qquad (11)$$

Moreover, in the assumed scenario featuring the same exterior medium at the two ends (see Fig. 1), the transmission coefficient of a finite-size metamaterial slab comprising n unit cells can be expressed as [17] (see also Appendix B for details)

$$\tau_n = \frac{2}{\chi_n + i\upsilon_n}. \qquad (12)$$

It is worth highlighting that, in view of the assumed lossless condition, the trace and antitrace in Eq. (10) are *real valued* [17]. If the number n of unit cells is varied, their evolution is governed by two iterated maps [17] (see also Appendix B for details),

$$\chi_n = \chi_1 \chi_{n-1} - \chi_{n-2}, \qquad (13a)$$

$$\upsilon_n = \chi_1 \upsilon_{n-1} - \upsilon_{n-2}, \quad n \geq 2, \qquad (13b)$$

which are coupled through the initial (unit-cell) trace χ_1. Remarkably, the above iterated maps admit a closed-form analytical solution as [17] (see also Appendix B for details)

$$\begin{aligned} \chi_n &= U_{n-1}\left(\frac{\chi_1}{2}\right) \chi_1 - 2U_{n-2}\left(\frac{\chi_1}{2}\right) \\ &= U_n\left(\frac{\chi_1}{2}\right) - U_{n-2}\left(\frac{\chi_1}{2}\right) = 2T_n\left(\frac{\chi_1}{2}\right), \end{aligned} \qquad (14a)$$

$$\upsilon_n = U_{n-1}\left(\frac{\chi_1}{2}\right) \upsilon_1, \qquad (14b)$$

with T_n and U_n denoting Chebyshev polynomials of the first and second kind, respectively (see Chap. 22 in [20]).

In spite of the different formalism adopted, the results in Eq. (12) [with Eqs. (14a) and (14b)] are exactly equivalent to those obtained via the conventional transfer-matrix method.

In what follows, we restrict our attention to the case $\chi_1 \leq 2$, which, recalling the dispersion relationship in Eq. (11), corresponds to the propagating condition (real-valued k_z) for the infinite multilayer. For finite-size structures, of direct interest in our study, by recalling Eq. (14a)

and that $|T_n(\xi)| \leq 1$ for $|\xi| \leq 1$ (see Eq. 22.14.4 in Ref. [20]), this also implies that

$$|\chi_n| \leq 2, \quad n \geq 1. \tag{15}$$

We stress that our assumption of identical exterior media at the two ends of the metamaterial does not imply a significant loss of generality in the description of the basic phenomena. If two different exterior media were assumed, as in Refs. [10,13,14], it would no longer be possible to express the transmission coefficient solely in terms of the trace and antitrace. Aside from the arising formal complications, this would not hinder the applicability of our approach, since it is possible to derive iterated maps for all the terms of the transfer matrix [17].

Moreover, it is worth highlighting that the above trace-and-antitrace-map formalism is not restricted to periodic multilayers, and can be extended to deal with rather general classes of *aperiodically ordered* structures generated by two-letter substitutional sequences (e.g., Fibonacci and Thue-Morse sequences) [17,21–23], although the arising iterated maps do not generally admit analytical, closed-form solutions.

III. BOUNDARY EFFECTS OF WEAK NONLOCALITY

A. Background

In Ref. [10], for the case $\varepsilon_e > \bar{\varepsilon}_\parallel$, it was observed that the agreement between the exact optical response of a finite-thickness multilayered metamaterial and the local EMT prediction would strongly deteriorate for incidence angles approaching the critical angle

$$\theta_c = \arcsin\left(\sqrt{\frac{\bar{\varepsilon}_\parallel}{\varepsilon_e}}\right), \tag{16}$$

which characterizes the total-internal-reflection condition between the exterior and effective media or, equivalently, the vanishing of the EMT-based longitudinal wavenumber $\bar{k}_z$ in Eq. (3). Assuming $\theta \lesssim \theta_c$, in view of Eq. (2), this regime implies that the field is propagating in the higher-permittivity layers and is evanescent in the lower-permittivity ones. In Ref. [14], an additional, independent mechanism was identified, leading to the breakdown of the standard EMT. This latter mechanism is not restricted to the critical-angle incidence above, but it is rather related to a phase mismatch at the interface separating the last layer and the exterior medium, and becomes particularly significant for $\varepsilon_e = \bar{\varepsilon}_\parallel$.

The breakdown of the local EMT model in the above scenarios is rather counterintuitive, as fully dielectric structures with deeply subwavelength inclusions are known to exhibit *negligibly weak* nonlocal effects. In fact,

such breakdown appears to be attributable to *boundary effects*, as it is manifested only in the transmission (and reflection) response of finite-size structures, whereas the *bulk* properties (dispersion relationship) are still accurately captured by the local EMT prediction [10,12].

B. Connection with the trace-and-antitrace-map formalism

To effectively model the phenomena described above, it is expedient to interpret the EMT homogenized structure as a fictitious multilayer composed of homogeneous unit cells of thickness d and relative permittivity $\bar{\varepsilon}_\parallel$ in Eq. (2). By comparing the traces and antitraces of the transfer matrices pertaining to the actual and homogenized unit cells, we obtain (see Appendix C for details)

$$\Delta\chi_1 = \chi_1 - \bar{\chi}_1 \approx -\frac{(kd)^4(\varepsilon_a - \varepsilon_b)^2 f_a^2 f_b^2}{12}, \tag{17a}$$

$$\Delta\upsilon_1 = \upsilon_1 - \bar{\upsilon}_1$$
$$\approx \frac{k(kd)^3(\varepsilon_a - \varepsilon_b)f_a f_b[(\varepsilon_a + \varepsilon_b - 2\varepsilon_e)f_b - \varepsilon_a + \varepsilon_e]}{6k_{ze}}, \tag{17b}$$

where, following the previously introduced notation, EMT-based quantities are indicated by an overbar. The errors in Eqs. (17a) and (17b) are manifestations of the inherent nonlocality of multilayered metamaterials. In structures such as hyperbolic metamaterials made of metallodielectric multilayers, these errors can be of sizable magnitude even for deeply subwavelength layers [6], thereby leading to strong bulk effects, such as additional extraordinary waves [24]. Conversely, for the case of *fully dielectric*, deeply subwavelength layers ($kd \ll 1$) of interest here, these errors are usually quite small, and are consequently expected to yield second-order effects. This is especially true for the trace error in Eq. (17a), whereas Eq. (17b) indicates that the antitrace error may become not so small for $k_{ze} \ll k$ (i.e., for near-grazing incidence from the exterior medium).

We recall, from Eq. (11), that the dispersion relationship depends solely on the initial (unit-cell) trace χ_1; this explains why, in the assumed conditions of deeply subwavelength dielectric layers, the EMT prediction of the *bulk* properties remains uniformly accurate even in the critical regimes observed in Refs. [10,12,14]. This is not necessarily the case for the transmission coefficient of a *finite-thickness* structure [cf. Eq. (12)], which instead depends on both the trace map and the antitrace map. Even in the case of *negligibly weak* nonlocality, resulting in very accurate approximations at the unit-cell level (i.e., $|\Delta\chi_1|, |\Delta\upsilon_1| \ll 1$), there is no guarantee that the errors will remain negligibly small as the iterations proceed (i.e.,
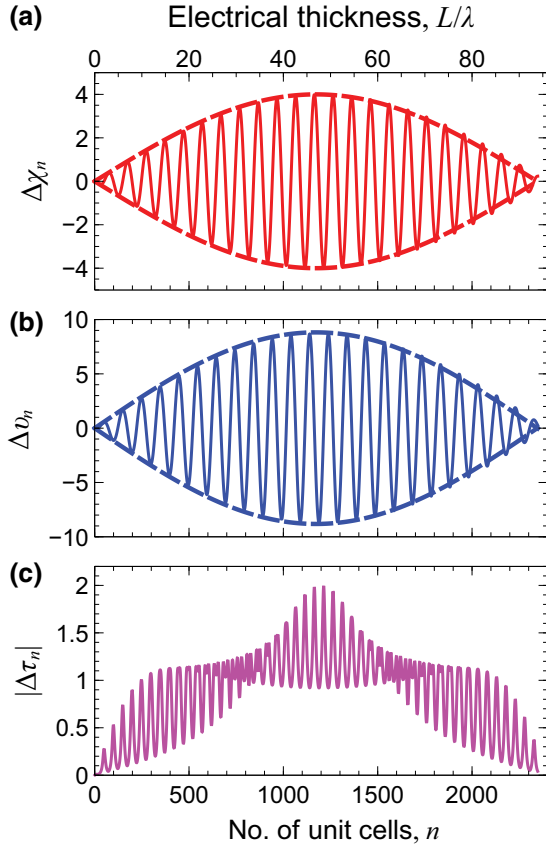
(a)

(b)

(c)

FIG. 2.   (a),(b) Trace and antitrace error maps [Eqs. (18a) and (18b), respectively] for a multilayer with $\varepsilon_a = 1$, $\varepsilon_b = 5$, $d_a = d_b = 0.02\lambda$ (i.e., $d = \lambda/25$, $f_a = f_b = 0.5$), an exterior medium with relative permittivity $\varepsilon_e = 4$, and near-critical incidence angle $\theta = 59°$. The solid curves indicate the rigorous reference solutions, whereas the dashed curves indicate the slowly varying envelopes from the leading terms in Eqs. (19a) and (19b). (c) Corresponding transmission-coefficient difference map [Eq. (18c)] computed via the rigorous reference solution. The results are shown as a function of the number of unit cells and corresponding electrical thickness L/λ (shown on the upper horizontal axis).

as the number of unit cells increases). This is the key observation behind our approach, from which it emerges that the boundary effects observed in Refs. [10,12,14] can be incisively interpreted and parameterized as an *error-propagation* problem in the trace and antitrace iterated maps. In particular, we show that the propagation effects of the initial (unit-cell) trace and antitrace errors ($\Delta\chi_1$ and $\Delta\upsilon_1$, respectively) are directly associated with the two distinct mechanisms identified in Refs. [10,14].

C. Analytical modeling

We define the error maps

$$\Delta\chi_n \equiv \chi_n - \bar{\chi}_n, \tag{18a}$$

$$\Delta\upsilon_n \equiv \upsilon_n - \bar{\upsilon}_n, \tag{18b}$$

$$\Delta\tau_n \equiv \tau_n - \bar{\tau}_n, \tag{18c}$$

which describe the propagation of the initial errors in Eqs. (17a) and (17b). In particular, for a metamaterial composed of n bilayers, $\Delta\tau_n$ quantifies the departure of the EMT-based approximation of the transmission coefficient from the exact (transfer-matrix-based) prediction. By assuming $|\Delta\chi_1|, |\Delta\upsilon_1| \ll 1$ and exploiting the analytical solutions in Eqs. (14a) and (14b) (see Appendix C for details), we obtain

$$\Delta\chi_n \approx X \sin(n\kappa) \sin(n\Omega), \tag{19a}$$

$$\Delta\upsilon_n \approx \Upsilon \cos(n\kappa) \sin(n\Omega) + \mathcal{O}(\Delta\chi_1, \Delta\upsilon_1), \tag{19b}$$

where $\mathcal{O}$ denotes the Landau "big-O" symbol, and

$$X = -4, \quad \Upsilon = 2\left(\frac{\bar{k}_z}{k_{ze}} + \frac{k_{ze}}{\bar{k}_z}\right), \tag{20}$$

$$\kappa = \bar{k}_z d + \mathcal{O}(\Delta\chi_1), \tag{21a}$$

$$\Omega = -\frac{\Delta\chi_1}{2\sqrt{4 - \bar{\chi}_1^2}} + \mathcal{O}(\Delta\chi_1^2) \approx \frac{(kd)^4 (\varepsilon_a - \varepsilon_b)^2 f_a^2 f_b^2}{48\bar{k}_z d}. \tag{21b}$$

We observe from Eqs. (19a), (19b), (20), (21a), and (21b) that the leading terms in the error maps depend on the initial (unit-cell) trace error $\Delta\chi_1$, whereas the initial antitrace error $\Delta\upsilon_1$ affects only the higher-order correction $\mathcal{O}(\Delta\chi_1, \Delta\upsilon_1)$ in Eq. (19b). Throughout the paper, we refer to these boundary effects as "type I" and "type II," respectively.

D. Type-I boundary effects

We start by considering the type-I boundary effects; that is, ignoring the higher-order correction $\mathcal{O}(\Delta\chi_1, \Delta\upsilon_1)$ in Eq. (19b) and focusing on the $\Delta\chi_1$-dependent leading terms. Under this assumption, we observe that the trace and antitrace errors propagate with oscillatory laws characterized by two scales (κ and Ω, identical for both) and two different amplitudes. Remarkably, both amplitudes *do not* depend on the initial (unit-cell) errors. More specifically, the trace error is always ≤ 4 in absolute value, irrespective of the incidence conditions and exterior medium, which is a direct consequence of the inherent trace bound in Eq. (15). Conversely, it is readily verified from Eq. (20) that the amplitude Υ of the antitrace error oscillations is always ≥ 4 and critically depends on the incidence conditions and exterior medium. In particular, it can become *arbitrarily large* in the two (opposite) limits $\bar{k}_z/k_{ze} \ll 1$ and $k_{ze}/\bar{k}_z \ll 1$. The former limit corresponds to the
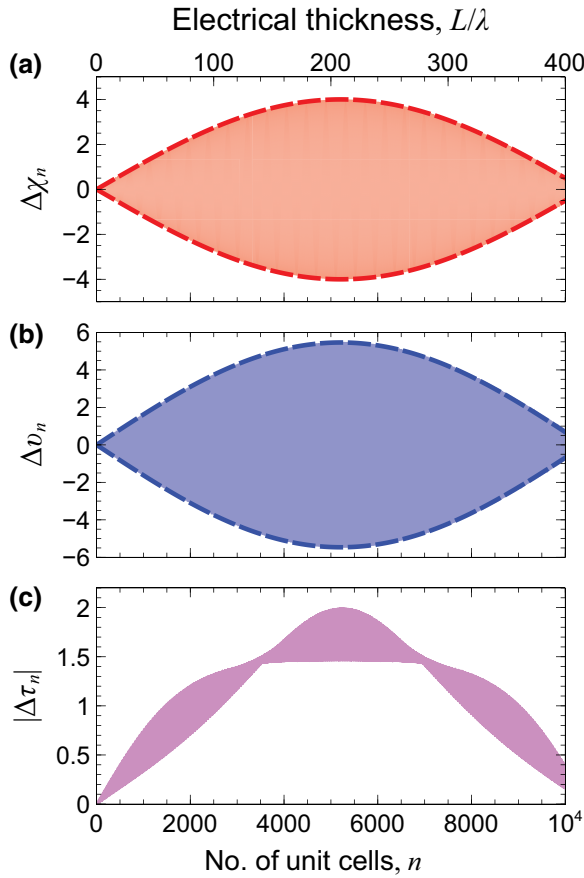
FIG. 3. As in Fig. 2 but with $\varepsilon_e = 2$ and $\theta = 70°$. The shaded areas are representative of the very fast oscillations, which are not individually distinguishable on the scale of the plots.
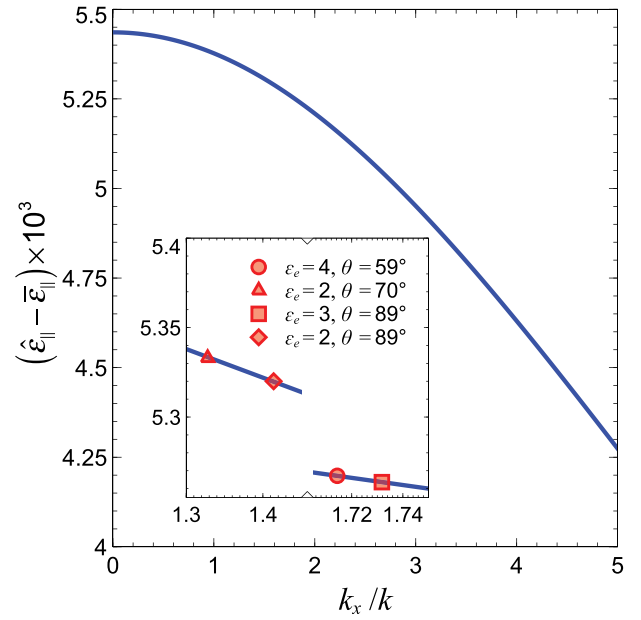

FIG. 4. Nonlocal correction [see Eq. (23)] on the conventional EMT model in Eq. (2) as a function of the (normalized) transverse wavenumber for a multilayer with $\varepsilon_a = 1$, $\varepsilon_b = 5$, $d_a = d_b = 0.02\lambda$ (i.e., $d = \lambda/25$, $f_a = f_b = 0.5$). Note the 10^3 scale factor on the vertical axis. The magnified view in the inset shows the parameter ranges of main interest (note the broken horizontal axis), with the circle, triangle, square, and diamond markers indicating the exterior-medium and incidence conditions considered in the various examples.

critical-angle-incidence condition [see Eq. (16)] explored in Ref. [10]. The latter limit, instead, becomes relevant when $\varepsilon_e < \bar{\varepsilon}_\parallel$ and, to the best of our knowledge, has not been observed and explored before. The above observations imply that, in their evolutions, the trace and antitrace error maps can exhibit peaks that are well beyond unity, which, via Eq. (12), translate into significant departures of the optical response from its EMT-based prediction (i.e., transmission-coefficient errors $\Delta\tau_n$ on the scale of unity).

Looking at the two scales that characterize the error oscillations, we observe from Eqs. (21a) and (21b) that κ essentially accounts for the phase accumulation in the EMT-homogenized medium, with a small correction on the order of $\Delta\chi_1$, whereas Ω directly depends on $\Delta\chi_1$, with a higher-order correction on the order of $(\Delta\chi_1)^2$ (see Appendix C for details). For typical parameter ranges of interest in this study, the two scales may be markedly different and, in particular, $\Omega \ll \kappa$. This yields a *slowly varying* envelope (ruled by Ω, and identical for both the trace error and the antitrace error modulated by fast oscillations (in quadrature, and ruled by κ). In this case, the

slow scale Ω is particularly meaningful to understand and parameterize the type-I boundary effects, and we can estimate from Eq. (21b) the critical size [i.e., the number of unit cells (apart from periodicities)]

$$n_p = \frac{\pi}{2\Omega} \approx \frac{24\pi \bar{k}_z d}{(kd)^4 (\varepsilon_a - \varepsilon_b)^2 f_a{}^2 f_b{}^2} \qquad (22)$$

around which the errors assume their peak values and, hence, the transmission-coefficient error (magnitude) $|\Delta\tau_n|$ is maximum. Likewise, it is apparent that for sizes of approximately $2n_p$ (plus periodicities) the errors tend to vanish.

We observe from Eq. (20) that the antitrace peak error Υ depends on the effective and exterior relative permittivities ($\bar{\varepsilon}_\parallel$ and ε_e, respectively) as well as on the incidence angle. However, it *does not* depend on how the metamaterial is synthesized—that is, the actual multilayer parameters (ε_a, ε_b, d/λ, f_a, and f_b)—and hence the degree on nonlocality. The degree on nonlocality, instead, plays a key role in establishing the critical size in Eq. (22). In other words, however weak the degree of nonlocality (i.e., however small $\Delta\chi_1$), once the desired effective and exterior permittivities and incidence conditions are set, a maximum
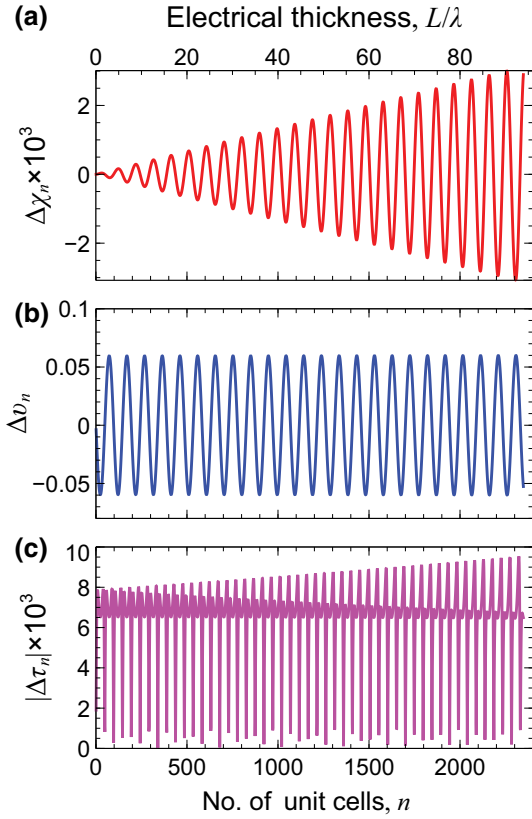
(a)

(b)

(c)

FIG. 5. As in Fig. 2 but considering the nonlocal effective model in Eq. (23). Note the 10^3 scale factors on the vertical axes in (a),(c).
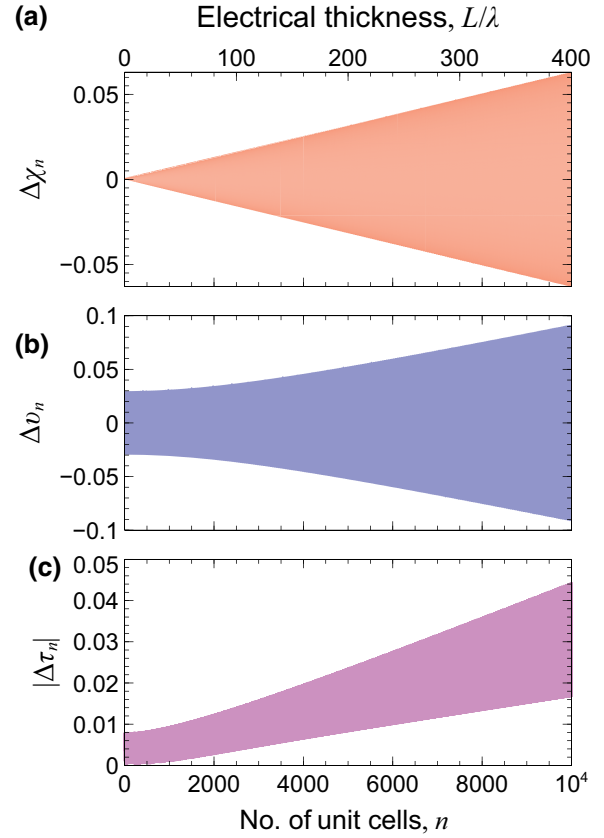
(a)

(b)

(c)

FIG. 6. As in Fig. 3 but considering the nonlocal effective model in Eq. (23). Also in this case, the shaded areas are representative of the very fast oscillations, which are not individually distinguishable on the scale of the plots.

potential strength of the type-I boundary effects is inherently established, which can become significantly large in certain critical conditions. The degree of nonlocality affects only the spatial scale for which the effects are manifested.

As an illustrative example, similarly to the study in Ref. [10], we consider a multilayered metamaterial with parameters $\varepsilon_a = 1$, $\varepsilon_b = 5$, and $d_a = d_b = 0.02\lambda$ (i.e., $f_a = f_b = 0.5$, $d = \lambda/25$). We start by considering a scenario featuring an exterior medium with $\varepsilon_e = 4$ and an incidence angle $\theta = 59°$ close to the critical angle [$\theta_c = 60°$, from Eq. (16)]. We observe that for this parameter configuration the initial (unit-cell) trace and antitrace errors are both very small ($\Delta\chi_1 = -3.32 \times 10^{-4}$ and $\Delta\upsilon_1 = -5.14 \times 10^{-3}$), and we therefore expect the leading terms in Eqs. (19a) and (19b) (i.e., type-I effects) to be dominant. Accordingly, since $\bar{k}_z/k_{ze} = 0.240$ (i.e., $\Upsilon \approx 8.82$), we expect sensible departures from the EMT predictions. Moreover, since $\Omega = 1.34 \times 10^{-3} \ll \kappa = 6.21 \times 10^{-2}$, we expect the fast-scale-slow-scale interpretation to hold.

Figure 2 illustrates the results pertaining to the error maps in Eqs. (18a) and (18b). As expected, the error maps exhibit a two-scale oscillatory behavior, in very good agreement with the predictions in Eqs. (19a) and (19b). In particular, although it takes about 1200 unit cells (i.e.,

$L \approx 50\lambda$) to reach the peak error, sensible departures from the EMT predictions may be observed also for hundreds of unit cells (i.e., $L \approx 5\lambda$). As shown in Fig. 2(c), this corresponds to transmission-coefficient (magnitude) errors on the scale of unity. For the same multilayer parameters as above, Fig. 3 shows some results pertaining to $\varepsilon_e = 2$ and $\theta = 70°$, representative of the somehow opposite regime ($\bar{k}_z/k_{ze} = 2.30$), which was not considered in previous studies. We observe that the initial trace error $\Delta\chi_1$ is the same as in the previous example (since it depends only on the multilayer parameters, which are not changed), whereas the antitrace error is different ($\Delta\upsilon_1 = -1.09 \times 10^{-2}$), but is still sufficiently small for the type-I effects to be dominant. Although total reflection is not possible in this scenario (since $\varepsilon_e < \bar{\varepsilon}_\parallel$), the field is still propagating in the higher-permittivity ("b"-type) layers and is still evanescent in the lower-permittivity ("a"-type) ones, and the type-I boundary effects still become visible for sufficiently large sizes ($n_p = 5275$). Since the fast scale is now almost 3 orders of magnitude larger than the slow scale ($\kappa = 937.7\Omega$), the fast oscillations are not individually distinguishable on the scale of the plots, and therefore we can observe only some shaded areas, whose envelopes are in
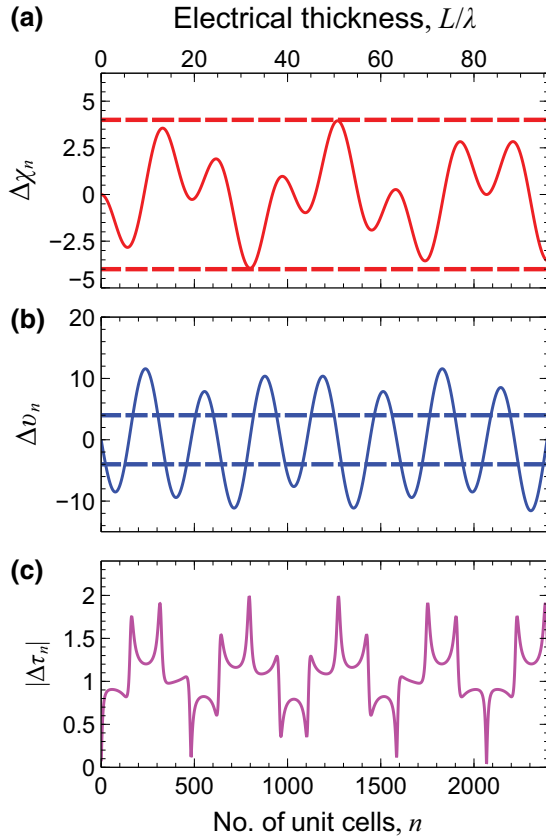
FIG. 7. As in Fig. 2 but with $\theta = 89°$ and $\varepsilon_e = 3$. The dashed lines in (a),(b) indicate the amplitude bounds [see Eq. (20)] predicted by the leading terms in Eqs. (19a) and (19b).

very good agreement with our approximate modeling in Eqs. (19a) and (19b). Other than that, the same observations as for the previous example hold.

E. Nonlocal corrections

The results above naturally suggest that the type-I boundary effects can be captured by a suitable nonlocal correction providing a more accurate approximation of the initial (unit-cell) trace error $\Delta \chi_1$.

To this aim, along the lines of the approach proposed in Ref. [6], we derive a *nonlocal* effective model (see Appendix D for details) in terms of a wavenumber-dependent relative permittivity

$$\hat{\varepsilon}_\parallel(k_x)$$
$$= \frac{6 + k_x^2 d^2 - \sqrt{36 + 12d^2(k_x^2 - k^2\bar{\varepsilon}_\parallel) + d^4(k_x^2 - \alpha_a k^2)(k_x^2 - \alpha_b k^2)}}{k^2 d^2},$$
(23)

with

$$\alpha_a = f_a^2 \varepsilon_a + f_b^2 \varepsilon_b + 2f_a f_b \varepsilon_a,$$ (24a)

$$\alpha_b = f_a^2 \varepsilon_a + f_b^2 \varepsilon_b + 2f_a f_b \varepsilon_b.$$ (24b)
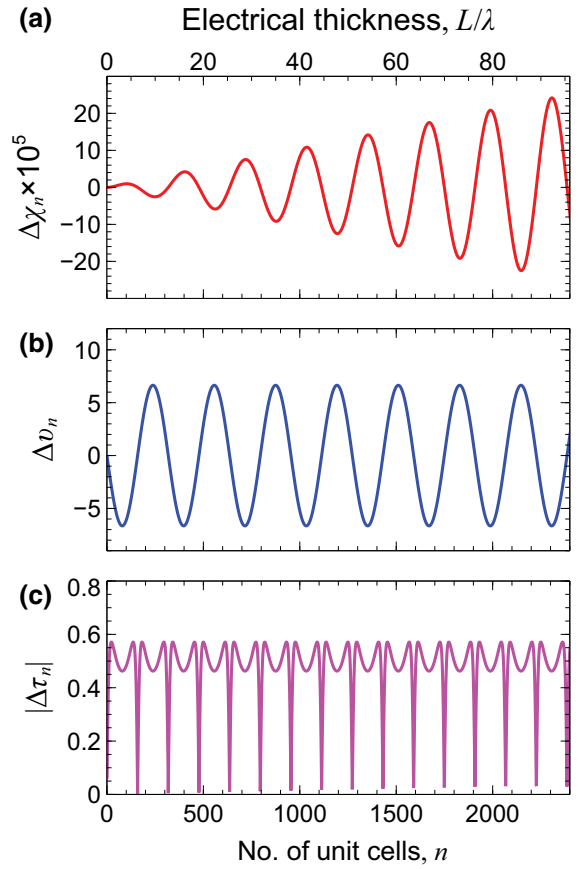

FIG. 8. As in Fig. 7 but considering the nonlocal effective model in Eq. (23). Note the 10^5 scale factor on the vertical axis in (a).

Here and henceforth, the caret is used to tag quantities related to the nonlocal effective model. It can be verified that in the limit $kd \to 0$ the nonlocal model in Eq. (23) consistently reduces to the conventional (local) EMT model in Eq. (2). As illustrated in Fig. 4, for the finite but small values of kd of interest here, the actual nonlocal corrections are very small (on the third decimal figure), thereby confirming the anticipated weak character. As a consequence, strong-nonlocality-induced effects such as additional extraordinary waves should not be expected, and there is no need to enforce additional boundary conditions when one is solving the boundary-value problem. For our specific case, it can be shown (see Appendix D for details) that the initial (unit-cell) trace error arising from Eq. (23) is given by

$$\Delta \chi_1 = \chi_1 - \hat{\chi}_1 \sim \mathcal{O}[(kd)^6(\varepsilon_a - \varepsilon_b)^2 f_a^2 f_b^2].$$ (25)

By comparison with the EMT-based counterpart in Eq. (17a), we observe a *much-faster* decrease (sixth power, instead of fourth) of the error with the unit-cell electrical
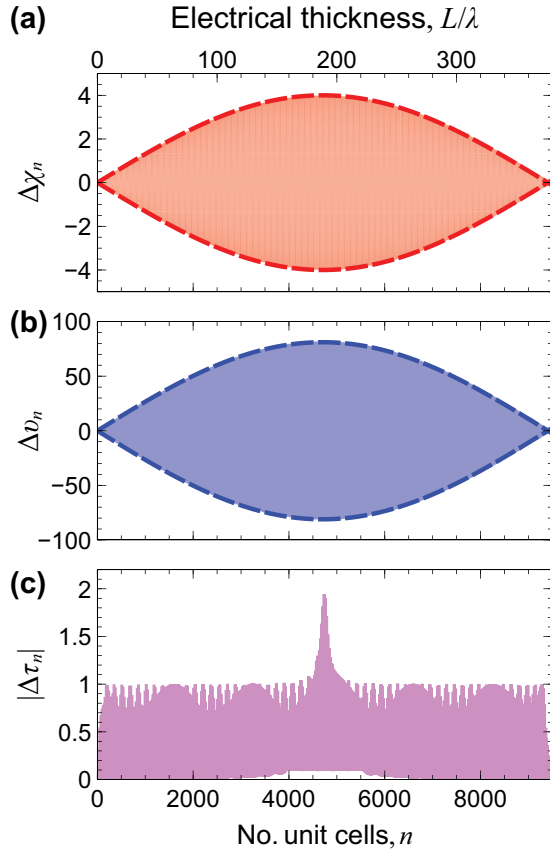
FIG. 9. As in Fig. 3 but with $\varepsilon_e = 2$ and $\theta = 89°$. Also in this case, the shaded areas are representative of the very fast oscillations, which are not individually distinguishable on the scale of the plots.
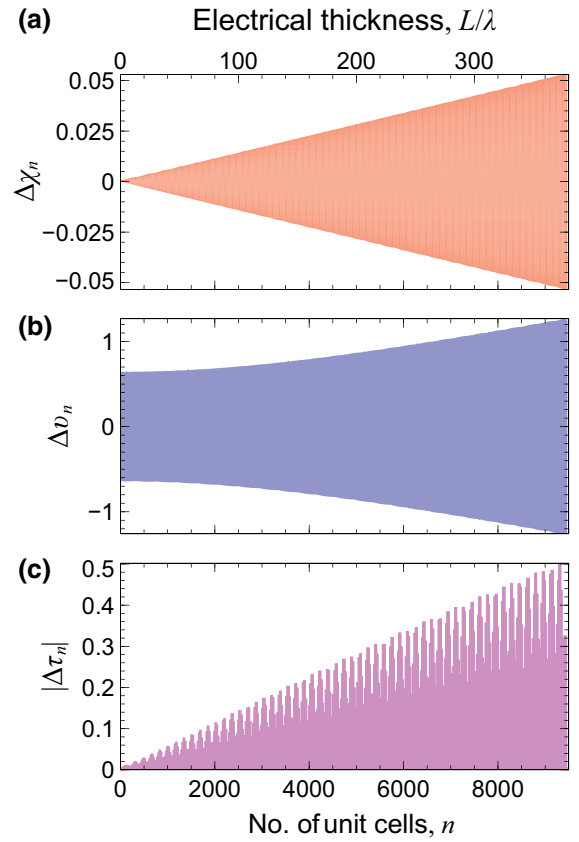

FIG. 10. As in Fig. 9 but considering the nonlocal effective model in Eq. (23). Also in this case, the shaded areas are representative of the very fast oscillations, which are not individually distinguishable on the scale of the plots.

thickness kd, which, in the regime of interest, potentially translates [via Eqs. (21b) and (22)] into orders-of-magnitude increases of the critical size for the boundary effects to manifest themselves.

As an illustrative example, Fig. 5 shows the results corresponding to the configuration in Fig. 2. For these parameters, the nonlocal effective model in Eq. (23) yields a 4-orders-of-magnitude-smaller initial trace error ($\Delta\chi_1 = 8.55 \times 10^{-8}$). As a consequence, on the same spatial scale of Fig. 2, both the trace error [Fig. 5(a)] and the antitrace error [Fig. 5(b)] are now strongly reduced, thereby yielding very small errors in the transmission coefficient [Fig. 5(c)].

Qualitatively similar results can be observed in Fig. 6 for the parameter configuration in Fig. 3.

Clearly, higher-order nonlocal corrections could be derived [6], which would further reduce the initial trace error $\Delta\chi_1$, and hence more accurately capture the arising type-I boundary effects. Alternatively, more-sophisticated nonlocal effective models could be used [9] that enforce the exact matching of the Bloch-type and effective dispersive relationships.

F. Type-II boundary effects

We now move on to consider the type-II boundary effects, which become relevant in scenarios where the initial (unit-cell) antitrace error $\Delta\upsilon_1$ and, hence, the higher-order correction term in Eq. (19b) are no longer negligibly small. From Eq. (17b), it is clear that this may happen, for instance, when $k_{ze} \ll k$ (i.e., for near-grazing incidence from the exterior medium). This is exemplified in Figs. 7 and 8 for a scenario with $\varepsilon_e = \bar{\varepsilon}_\parallel = 3$ and $\theta = 89°$, for which $\Delta\chi_1$ remains negligibly small but $\Delta\upsilon_1 = -0.18$ is no longer negligible. More specifically, Fig. 7 shows the error maps pertaining to the standard (local) EMT model. Unlike the previous examples (see Figs. 2 and 3), we can no longer interpret the oscillatory behaviors of the trace and antitrace errors in terms of fast oscillations and a slow envelope, since the two scales are actually inverted ($\kappa < \Omega$) and rather close in value ($\kappa = 7.60 \times 10^{-3}$, $\Omega = 1.09 \times 10^{-2}$). Nevertheless, the trace error [Fig. 7(a)] still satisfies the amplitude bound implied by Eq. (19a). Conversely, we observe from Fig. 7(b) that the antitrace error may exceed (by more than a factor of 2) the amplitude bound predicted by Υ

in Eq. (20). As expected, these boundary effects are no longer accurately captured by the leading terms in Eqs. (19a) and (19b).

Figure 8 shows instead the corresponding results obtained by our considering the nonlocal effective model in Eq. (23). We observe that the trace error [Fig. 8(a)] is now substantially reduced, but the antitrace error [Fig. 8(b)] still exhibits moderately large (> 5) peak values. As a result, the transmission-coefficient error [Fig. 8(c)] can still reach values of approximately 0.6 in magnitude, even for relatively small sizes, thereby indicating that these boundary effects are not even captured very accurately by the nonlocal correction. This should not be surprising, as the nonlocal effective model in Eq. (23) was derived with the aim of reducing the initial trace error ($\Delta \chi_1$) only, and it does not affect the initial antitrace error $\Delta \upsilon_1$ responsible for the type-II boundary effects.

Another insightful example is illustrated in Figs. 9 and 10 for a scenario with $\varepsilon_e = 2$ and $\theta = 89°$. In this case the initial antitrace error $\Delta \upsilon_1 = -0.21$, albeit not small in absolute terms, remains negligible by comparison with the quite large amplitude of the leading term ($\Upsilon = 81$). In other words, in this regime the type-I boundary effects are still dominant. As a result, we observe from Fig. 9 that the leading terms in Eqs. (19a) and (19b) still provide an accurate modeling. However, as clearly exemplified in Fig. 10, when the nonlocal effective model is applied, and hence the type-I effects are accurately captured, the residual type-II effects become clearly visible. The two examples above clearly indicate the different and independent nature of the type-II boundary effects. For the scenario $\varepsilon_e \geq \bar{\varepsilon}_\parallel$, a similar additional mechanism was identified in Ref. [14]. Such a phenomenon, not restricted to the critical-angle incidence and particularly significant for $\varepsilon_e = \bar{\varepsilon}_\parallel$, was explained in terms of a phase mismatch at the interface separating the last layer and the exterior medium. Remarkably, it was concluded that the effect could not be captured by local and nonlocal homogenization in terms of a *single* effective layer, and the addition of an artificial matched layer was required.

Our results indicate that such boundary effects may also become dominant in scenarios with $\varepsilon_e < \bar{\varepsilon}_\parallel$. Moreover, they also indicate that a *single-parameter* nonlocal effective model is generally not sufficient to capture these effects. More complex (multiparameter) extensions are required to more accurately approximate the initial (unit-cell) values of both the trace and antitrace. However, since the antitrace (unlike the trace) inherently depends on the exterior medium, the simplest conceivable extension, entailing the introduction of a (wavenumber-dependent) effective magnetic permeability would also inherit such dependence, thereby leading to a model inconsistency. A self-consistent model, with effective parameters independent of the exterior medium, should correctly approximate *all* the transfer-matrix terms. This would inevitably entail some magnetoelectric coupling, along the lines of the approach in Ref. [13]. We regard this further development as beyond the scope of the present investigation.

IV. CONCLUSIONS AND OUTLOOK

We apply the trace-and-antitrace-map formalism to model the boundary effects induced by weak nonlocality in multilayered metamaterials made of periodic stacks of alternating, deeply subwavelength dielectric layers.

Our approach naturally identifies two distinct boundary effects, associated with different error-propagation effects in the trace and antitrace maps. Moreover, it leads to some analytical models that naturally highlight the critical parameters and conditions (including some not considered in previous studies), and provide very useful insights in the development of nonlocal corrections. Overall, we believe that our results nicely complement previous studies on these phenomena [10,13,14] by offering a different perspective and paving the way to intriguing extensions.

For instance, our approach can be fruitfully extended to *aperiodically ordered* multilayers [17,21–23] so as to explore the effects induced by the spatial arrangement. Because of the more-complex character of the arising maps, the trace bound in Eq. (15) would not necessarily hold in these scenarios, thereby giving rise to richer dynamics involving transitions between propagating and evanescent regimes. Within a related framework, also of great interest are possible applications to the study of Anderson localization effects in random multilayers, along the lines of Refs. [15,16].

Finally, also worthy of mention are possible extensions to non-Hermitian scenarios featuring balanced loss and gain, which are experiencing a surging interest in optics and photonics (see, e.g., Ref. [25] for a recent review). Within this framework, we observe that under the special conditions of *parity-time* symmetry [26] for the unit cell ($\varepsilon_a = \varepsilon_b^*$, $d_a = d_b$), the trace and antitrace maps remain *real valued*, thereby greatly simplifying the study and interpretation of the phenomena. Moreover, since the conventional EMT model of a parity-time-symmetric multilayer would yield a lossless (and gainless) effective medium, the phenomena studied here are expected to be closely related to distinctive effects that can occur in non-Hermitian systems, such as the emergence of *exceptional points* [27].

APPENDIX A: DETAILS ON THE TRANSFER-MATRIX FORMALISM

Following Chap. 1 in Ref. [18], the transfer matrices pertaining to the single layers can be expressed as

$$\underline{\underline{\mathcal{M}}}_a = \begin{bmatrix} \cos(k_{za}f_a d) & \dfrac{k_{ze}}{k_{za}}\sin(k_{za}f_a d) \\ -\dfrac{k_{za}}{k_{ze}}\sin(k_{za}f_a d) & \cos(k_{za}f_a d) \end{bmatrix}, \quad (A1a)$$

$$\underline{\underline{\mathcal{M}}}_b = \begin{bmatrix} \cos(k_{zb}f_b d) & \dfrac{k_{ze}}{k_{zb}}\sin(k_{zb}f_b d) \\ -\dfrac{k_{zb}}{k_{ze}}\sin(k_{zb}f_b d) & \cos(k_{zb}f_b d) \end{bmatrix}, \quad (A1b)$$

where $k_{za} = \sqrt{k^2\varepsilon_a - k_x^2}$ and $k_{zb} = \sqrt{k^2\varepsilon_b - k_x^2}$ denote the longitudinal wavenumbers in the two corresponding media, and all other symbols are defined in the main text. By multiplication of the two matrices above, the unit-cell trace and antitrace are straightforwardly obtained as [see Eq. (10) with $n = 1$]

$$\chi_1 = 2\cos(k_{za}f_a d)\cos(k_{zb}f_b d)$$
$$- \left(\frac{k_{za}}{k_{zb}} + \frac{k_{zb}}{k_{za}}\right)\sin(k_{za}f_a d)\sin(k_{zb}f_b d), \quad (A2a)$$

$$\upsilon_1 = -\left(\frac{k_{za}}{k_z} + \frac{k_z}{k_{za}}\right)\sin(k_{za}f_a d)\cos(k_{zb}f_b d)$$
$$- \left(\frac{k_{zb}}{k_z} + \frac{k_z}{k_{zb}}\right)\cos(k_{za}f_a d)\sin(k_{zb}f_b d). \quad (A2b)$$

APPENDIX B: DETAILS ON THE TRACE AND ANTITRACE MAPS

Assuming we have a generic transfer matrix $\underline{\underline{\mathcal{M}}}$ (see the inset in Fig. 1) and unit-amplitude, TE-polarized plane-wave incidence, the input and output electric fields can be written as

$$E_y^{(i)} = \exp(ik_x x)\left[\exp(ik_{ze}z) + \Gamma\exp(-ik_{ze}z)\right], \quad (B1a)$$

$$E_y^{(o)} = \tau\exp\{i[k_x x + k_{ze}(z - L)]\}, \quad (B1b)$$

where Γ and τ denote the reflection and transmission coefficients, respectively. By computing the corresponding magnetic field tangential components via the relevant Maxwell's curl equation, and substituting them in Eq. (4), we obtain the linear system

$$\begin{bmatrix} 1 + \Gamma \\ -i(1 - \Gamma) \end{bmatrix} = \underline{\underline{\mathcal{M}}} \cdot \begin{bmatrix} \tau \\ -i\tau \end{bmatrix}, \quad (B2)$$

which, solved with respect to τ, yields

$$\tau = \frac{2}{\mathcal{M}_{11} + \mathcal{M}_{22} + i(\mathcal{M}_{21} - \mathcal{M}_{12})}. \quad (B3)$$

Equation (12) directly follows from Eq. (B3) by our particularizing $\underline{\underline{\mathcal{M}}} = \underline{\underline{\mathcal{M}}}_{ab}^n$ and recalling the trace and antitrace definitions in Eq. (9).

As a consequence of the Cayley-Hamilton theorem [19], the square of a 2×2 unimodular matrix can be expressed as [22]

$$\underline{\underline{\mathcal{M}}}^2 = \mathrm{Tr}\left(\underline{\underline{\mathcal{M}}}\right)\underline{\underline{\mathcal{M}}} - \underline{\underline{\mathcal{I}}}, \quad (B4)$$

with $\underline{\underline{\mathcal{I}}}$ denoting the 2×2 identity matrix. The trace and antitrace maps in Eq. (13) are obtained from Eq. (B4), particularized for $\underline{\underline{\mathcal{M}}} = \underline{\underline{\mathcal{M}}}_{ab}$, by our multiplying both sides by $\underline{\underline{\mathcal{M}}}^{n-2}$ (with $n \geq 2$) and calculating the trace and antitrace, respectively.

Via recursive application of Eq. (B4), we also obtain [22]

$$\underline{\underline{\mathcal{M}}}^n = U_{n-1}\left[\frac{1}{2}\mathrm{Tr}\left(\underline{\underline{\mathcal{M}}}\right)\right]\underline{\underline{\mathcal{M}}} - U_{n-2}\left[\frac{1}{2}\mathrm{Tr}\left(\underline{\underline{\mathcal{M}}}\right)\right]\underline{\underline{\mathcal{I}}}, \quad (B5)$$

from which the analytical solutions in Eqs. (14a) and (14b) directly follow by our particularizing $\underline{\underline{\mathcal{M}}} = \underline{\underline{\mathcal{M}}}_{ab}$ and calculating the trace and antitrace.

APPENDIX C: DERIVATION OF EQS. (17a), (17b), (19a), AND (19b)

First, we derive the approximations in Eqs. (17a) and (17b) for the initial (unit-cell) trace and antitrace errors. By expanding Eq. (A2a) in a Maclaurin series with respect to d (up to the fourth order), we obtain

$$\chi_1 \approx 2 - (\bar{k}_z d)^2 + \frac{d^4}{12}\left[k_x^2 - k^2\left(f_a^2\varepsilon_a + f_b^2\varepsilon_b + 2f_a f_b\varepsilon_a\right)\right]$$
$$\left[k_x^2 - k^2\left(f_a^2\varepsilon_a + f_b^2\varepsilon_b + 2f_a f_b\varepsilon_b\right)\right]. \quad (C1)$$

Recalling the transfer matrix of the EMT-homogenized medium,

$$\underline{\underline{\bar{\mathcal{M}}}} = \begin{bmatrix} \cos(\bar{k}_z d) & \dfrac{k_{ze}}{\bar{k}_z}\sin(\bar{k}_z d) \\ -\dfrac{\bar{k}_z}{k_{ze}}\sin(\bar{k}_z d) & \cos(\bar{k}_z d) \end{bmatrix}, \quad (C2)$$

we obtain likewise (for $\bar{k}_z d \ll 1$)

$$\bar{\chi}_1 = 2\cos\left(\bar{k}_z d\right) \approx 2 - \left(\bar{k}_z d\right)^2 + \frac{\left(\bar{k}_z d\right)^4}{12}. \quad (C3)$$

The approximation in Eq. (17a) follows by our subtracting Eqs. (C1) and (C3) and recalling Eq. (3).

In a similar fashion, via Maclaurin expansions of υ_1 and $\bar{\upsilon}_1$ (up to the third order in d), we obtain

$$
\begin{aligned}
\upsilon_1 \approx \frac{d}{6k_{ze}} \Big\{ &f_a \left[k^2 \left(\varepsilon_e + \varepsilon_a \right) - 2k_x^2 \right] \left(k_{za}^2 d^2 f_a^2 - 6 \right) \\
&+ 3f_b \left[k^2 \left(\varepsilon_e + \varepsilon_b \right) - 2k_x^2 \right] \left(k_{za}^2 d^2 f_a^2 - 2 \right) \\
&+ 3k_{zb}^2 d^2 f_a f_b^2 \left[k^2 \left(\varepsilon_e + \varepsilon_a \right) - 2k_x^2 \right] \\
&+ k_{zb}^2 d^2 f_b^3 \left[k^2 \left(\varepsilon_e + \varepsilon_b \right) - 2k_x^2 \right] \Big\},
\end{aligned}
\tag{C4}
$$

$$
\begin{aligned}
\bar{\upsilon}_1 &= - \left(\frac{\bar{k}_z}{k_{ze}} + \frac{k_{ze}}{\bar{k}_z} \right) \sin \left(\bar{k}_z d \right) \\
&\approx \frac{d \left[\left(\bar{\varepsilon}_\parallel + \varepsilon_e \right) k^2 - 2k_x^2 \right] \left(\bar{k}_z^2 d^2 - 6 \right)}{6k_{ze}},
\end{aligned}
\tag{C5}
$$

which, after some algebra, yield the approximation in Eq. (17b).

From Eq. (18a), by recalling the trigonometric form of the Chebyshev polynomials of the first kind (see Eq. 22.3.15 in Ref. [20]), we obtain

$$
\begin{aligned}
\Delta\chi_n &= 2 \Bigg\{ \cos \left[n \arccos \left(\frac{\bar{\chi}_1 + \Delta\chi_1}{2} \right) \right] \\
&\quad - \cos \left[n \arccos \left(\frac{\bar{\chi}_1}{2} \right) \right] \Bigg\} \\
&= -4 \sin \left\{ \frac{n}{2} \left[\arccos \left(\frac{\bar{\chi}_1 + \Delta\chi_1}{2} \right) \right.\right. \\
&\quad \left.\left. + \arccos \left(\frac{\bar{\chi}_1}{2} \right) \right] \right\} \\
&\quad \times \sin \left\{ \frac{n}{2} \left[\arccos \left(\frac{\bar{\chi}_1 + \Delta\chi_1}{2} \right) \right.\right. \\
&\quad \left.\left. - \arccos \left(\frac{\bar{\chi}_1}{2} \right) \right] \right\},
\end{aligned}
\tag{C6}
$$

where a sum-to-product identity (see Eq. 4.3.37 in Ref. [20]) was used in the second equality. Next, under the assumption $\Delta\chi_1 \ll 1$, we apply the following approximations:

$$
\begin{aligned}
&\arccos \left(\frac{\bar{\chi}_1 + \Delta\chi_1}{2} \right) + \arccos \left(\frac{\bar{\chi}_1}{2} \right) \\
&\approx 2 \arccos \left(\frac{\bar{\chi}_1}{2} \right) - \frac{\Delta\chi_1}{\sqrt{4 - \chi_1^2}},
\end{aligned}
\tag{C7a}
$$

$$
\begin{aligned}
&\arccos \left(\frac{\bar{\chi}_1 + \Delta\chi_1}{2} \right) - \arccos \left(\frac{\bar{\chi}_1}{2} \right) \\
&\approx -\frac{\Delta\chi_1}{\sqrt{4 - \chi_1^2}} - \frac{\chi_1 \left(\Delta\chi_1 \right)^2}{2\sqrt{\left(4 - \chi_1^2 \right)^3}},
\end{aligned}
\tag{C7b}
$$

which, substituted in Eq. (C6), yield the parameterization in Eq. (19a), with the expression of κ and Ω in Eqs. (21a) and (21b) obtained by our recalling [from Eq. (17a)] that

$$
\bar{\chi}_1 = 2 \cos \left(\bar{k}_z d \right),
\tag{C8}
$$

and that, for $\bar{k}_z d \ll 1$,

$$
\sqrt{4 - \bar{\chi}_1^2} = 2 \sin \left(\bar{k}_z d \right) \approx 2\bar{k}_z d.
\tag{C9}
$$

Moving on to the antitrace error map in Eq. (18b), by recalling the trigonometric form of the Chebyshev polynomials of the second kind [see Eq. 22.3.16 in Ref. [20]], we obtain

$$
\begin{aligned}
\Delta\upsilon_n &= \frac{2 \left(\bar{\upsilon}_1 + \Delta\upsilon_1 \right) \sin \left[n \arccos \left(\frac{\bar{\chi}_1 + \Delta\chi_1}{2} \right) \right]}{\sqrt{4 - \left(\bar{\chi}_1 + \Delta\chi_1 \right)^2}} \\
&\quad - \frac{2\bar{\upsilon}_1 \sin \left[n \arccos \left(\frac{\bar{\chi}_1}{2} \right) \right]}{\sqrt{4 - \bar{\chi}_1^2}}.
\end{aligned}
\tag{C10}
$$

Then, in the limit $|\Delta\chi_1|, |\Delta\upsilon_1| \ll 1$, we use the approximation

$$
\begin{aligned}
\frac{2 \left(\bar{\upsilon}_1 + \Delta\upsilon_1 \right)}{\sqrt{4 - \left(\bar{\chi}_1 + \Delta\chi_1 \right)^2}} &\approx \frac{2\bar{\upsilon}_1}{\sqrt{4 - \bar{\chi}_1^2}} + \frac{2\Delta\bar{\upsilon}_1}{\sqrt{4 - \bar{\chi}_1^2}} \\
&\quad + \frac{2\bar{\chi}_1 \bar{\upsilon}_1 \Delta\chi_1}{\sqrt{\left(4 - \bar{\chi}_1^2 \right)^3}},
\end{aligned}
\tag{C11}
$$

which, substituted in Eq. (C10), yields the parameterization in Eq. (19b) by or applying the same approximations as in Eqs. (C7a) and (C7) and recalling that [from Eqs. (C5) and (C7)]

$$
\frac{2\bar{\upsilon}_1}{\sqrt{4 - \bar{\chi}_1^2}} = - \left(\frac{\bar{k}_z}{k_{ze}} + \frac{k_{ze}}{\bar{k}_z} \right).
\tag{C12}
$$

APPENDIX D: DERIVATION OF EQ. (23)

Our nonlocal homogenization strategy is inspired by the approach put forward in Ref. [6]. First, similarly to the derivation of Eq. (C3), we expand the trace of the transfer matrix of the nonlocally homogenized unit cell as

$$
\hat{\chi}_1 = 2 \cos \left(\hat{k}_z d \right) \approx 2 - \left(\hat{k}_z d \right)^2 + \frac{\left(\hat{k}_z d \right)^4}{12},
\tag{D1}
$$

where

$$
\hat{k}_z = \sqrt{k^2 \hat{\varepsilon}_\parallel \left(k_x \right) - k_x^2},
\tag{D2}
$$

and, following the notation introduced in the main text, the caret denotes quantities based on nonlocal homogenization. The basic idea is to choose the function $\hat{\varepsilon}_\parallel(k_x)$ so as to enforce the matching between Eqs. (D1) and (C1) up to the fourth order in d. After some algebra, this yields a quadratic equation in $\hat{\varepsilon}_\parallel^2$; viz.,

$$k^2 d^2 \hat{\varepsilon}_\parallel^2(k_x) - 2(6 + k_x^2 d^2)\hat{\varepsilon}_\parallel(k_x) + 2(6 + k_x^2 d^2)\bar{\varepsilon}_\parallel$$
$$- k^2 d^2 \alpha_a \alpha_b = 0, \qquad (D3)$$

with the coefficients α_a and α_b defined in Eqs. (24a) and (24b). Of the two possible solutions, one turns out to be physically inconsistent, as it diverges in the limit $kd \to 0$. We are therefore left with the solution in Eq. (23), which consistently reduces to the standard (local) EMT model (2) in the above limit. This yields an initial (unit-cell) trace error

$$\Delta\chi_1 = \chi_1 - \hat{\chi}_1 \approx \frac{(kd)^6 (\varepsilon_a - \varepsilon_b)^2 f_a^2 f_b^2}{360}$$
$$\times \{3\varepsilon_a + f_b [\varepsilon_b - 5\varepsilon_a + 2f_b (\varepsilon_a + \varepsilon_b)]$$
$$+ \left(\frac{k_x}{k}\right)^2 (4f_a f_b - 3)\Bigg\}, \qquad (D4)$$

as compactly indicated in Eq. (25).

---

[1] D. Landau and E. M. Lifshitz, *Electrodynamics of Continuous Media* (Pergamon Press, New York, 1960).

[2] F. Capolino, *Theory and Phenomena of Metamaterials* (CRC Press, Boca Raton, FL, 2009).

[3] W. Cai and V. M. Shalaev, *Optical Metamaterials: Fundamentals and Applications* (Springer, New York, 2010).

[4] A. Sihvola, *Electromagnetic Mixing Formulas and Applications*, Electromagnetics and Radar Series (IET, London, UK, 1999).

[5] M. G. Silveirinha, Metamaterial homogenization approach with application to the characterization of microstructured composites with negative parameters, Phys. Rev. B **75**, 115104 (2007).

[6] J. Elser, V. A. Podolskiy, I. Salakhutdinov, and I. Avrutsky, Nonlocal effects ineffective-medium response of nanolayered metamaterials, Appl. Phys. Lett. **90**, 191109 (2007).

[7] A. Alù, First-principles homogenization theory for periodic metamaterials, Phys. Rev. B **84**, 075153 (2011).

[8] A. V. Chebykin, A. A. Orlov, A. V. Vozianova, S. I. Maslovski, Y. S. Kivshar, and P. A. Belov, Nonlocal effective medium model for multilayered metal-dielectric metamaterials, Phys. Rev. B **84**, 115438 (2011).

[9] A. V. Chebykin, A. A. Orlov, C. R. Simovski, Y. S. Kivshar, and P. A. Belov, Nonlocal effective parameters of multilayered metal-dielectric metamaterials, Phys. Rev. B **86**, 115420 (2012).

[10] H. Herzig Sheinfux, I. Kaminer, Y. Plotnik, G. Bartal, and M. Segev, Subwavelength Multilayer Dielectrics: Ultrasensitive Transmission and Breakdown of Effective-Medium Theory, Phys. Rev. Lett. **113**, 243901 (2014).

[11] A. Andryieuski, A. V. Lavrinenko, and S. V. Zhukovsky, Anomalous effective medium approximation breakdown in deeply subwavelength all-dielectric photonic multilayers, Nanotechnology **26**, 184001 (2015).

[12] S. V. Zhukovsky, A. Andryieuski, O. Takayama, E. Shkondin, R. Malureanu, F. Jensen, and A. V. Lavrinenko, Experimental Demonstration of Effective Medium Approximation Breakdown in Deeply Subwavelength All-Dielectric Multilayers, Phys. Rev. Lett. **115**, 177402 (2015).

[13] V. Popov, A. V. Lavrinenko, and A. Novitsky, Operator approach to effective medium theory to overcome a breakdown of Maxwell Garnett approximation, Phys. Rev. B **94**, 085428 (2016).

[14] X. Lei, L. Mao, Y. Lu, and P. Wang, Revisiting the effective medium approximation in all-dielectric subwavelength multilayers: Breakdown and rebuilding, Phys. Rev. B **96**, 035439 (2017).

[15] H. Herzig Sheinfux, I. Kaminer, A. Z. Genack, and M. Segev, Interplay between evanescence and disorder in deep subwavelength photonic structures, Nat. Commun. **7**, 12927 (2016).

[16] H. Herzig Sheinfux, Y. Lumer, G. Ankonina, A. Z. Genack, G. Bartal, and M. Segev, Observation of Anderson localization in disordered nanophotonic structures, Science **356**, 953 (2017).

[17] X. Wang, U. Grimm, and M. Schreiber, Trace and antitrace maps for aperiodic sequences: Extensions and applications, Phys. Rev. B **62**, 14020 (2000).

[18] M. Born and E. Wolf, *Principles of Optics* (Cambridge University Press, Cambridge, UK, 1999), 7th ed.

[19] S. Lang, *Linear Algebra* (Springer, Berlin, 1987), 3rd ed.

[20] M. Abramowitz and I. A. Stegun, *Handbook of Mathematical Function: With Formulas Graphs, and Mathematical Tables* (Dover, New York, 1965).

[21] M. Kolárr and F. Nori, Trace maps of general substitutional sequences, Phys. Rev. B **42**, 1062 (1990).

[22] M. Kolárr and M. K. Ali, Trace maps associated with general two-letter substitution rules, Phys. Rev. A **42**, 7112 (1990).

[23] S. Savoia, G. Castaldi, and V. Galdi, Optical nonlocality in multilayered hyperbolic metamaterials based on Thue-Morse superlattices, Phys. Rev. B **87**, 235116 (2013).

[24] A. A. Orlov, P. M. Voroshilov, P. A. Belov, and Y. S. Kivshar, Engineered optical nonlocality in nanostructured metamaterials, Phys. Rev. B **84**, 045424 (2011).

[25] L. Feng, R. El-Ganainy, and L. Ge, Non-Hermitian photonics based on parity-time symmetry, Nat. Photonics **11**, 752 (2017).

[26] C. M. Bender and S. Boettcher, Real Spectra in Non-Hermitian Hamiltonians Having *PT* Symmetry, Phys. Rev. Lett. **80**, 5243 (1998).

[27] W. D. Heiss, The physics of exceptional points, J. Phys. A: Math. Theor. **45**, 444016 (2012).